Journal of Luminescence 220 (2020) 116990

Contents lists available at ScienceDirect

Journal of Luminescence

journal homepage: http://www.elsevier.com/locate/jlumin

Towards a white-emitting phosphor $Ca_{10}V_6O_{25}$ based material

Mayara Mondego Teixeira [a], Yara Galvão Gobato [b,c], Lourdes Gracia [d,1], Luís Fernando da Silva [b], Waldir Avansi Jr. [b], Marcelo Assis [a], Regiane Cristina de Oliveira [e], Gabriela Augusta Prando [b], Juan Andrés [d], Elson Longo [a,*]

[a] CDMF-UFSCar, Universidade Federal de São Carlos, P.O. Box 676, 13565-905, São Carlos, SP, Brazil
[b] Departamento de Física, Universidade Federal de São Carlos, Rod. Washington Luiz, km 235, CP 676, CEP 13565-905, São Carlos, SP, Brazil
[c] High Fields Magnetic Laboratory, Radboud University, Toernooiveld 7, 6525 ED, Nijmegen, Netherlands
[d] Departamento de Química Física i Analítica, Universitat Jaume I, 12071, Castelló de la Plana, Spain
[e] Grupo de Modelagem e Simulações Moleculares, Faculdade de Ciências, Universidade Estadual de São Paulo, Bauru, SP, Brazil

ARTICLE INFO

Keywords:
Calcium vanadate $Ca_{10}V_6O_{25}$
White emission
Thermal quenching
Optical properties

ABSTRACT

To achieve a stable material capable of white-light emission, we fabricated $Ca_{10}V_6O_{25}$ by both co-precipitation (CP) and microwave-assisted hydrothermal (MAH) methods at different temperatures. The effects of structural disorder at a short-range (Raman spectra), medium-range (UV–vis spectra), and long-range (X-ray diffraction) on the material structure and its effect on optical properties were investigated. Both CP and the MAH methods were efficient for obtaining pure $Ca_{10}V_6O_{25}$ material with different morphologies. Significant changes in morphology and degree of structural order and disorder were found to affect the photoluminescence (PL) properties. All samples exhibited a broadband PL spectrum, characteristic associated to charge transfer processes of the $[VO_4]^{3-}$ group, as well as transitions that occurred in the energy levels located within the band gap. The samples obtained by the MAH method at temperatures of 100 °C and 120 °C exhibited a lower structural disorder (at long- and short-ranges), the CIE chromaticity coordinates were located in the white region, MAH100 (x = 0.311 and y = 0.348) and MAH120 (x = 0.350 and y = 0.368). Furthermore, we conducted a detailed study of temperature dependence of PL spectra. All samples displayed decreased luminescence intensity as temperatures increased and low values of activation energy (approximately 2 meV). Finally, the as-synthetized $Ca_{10}V_6O_{25}$ material has interesting properties for possible applications as a white-emitting phosphor under ultraviolet excitation.

1. Introduction

The intrinsic characteristics of vanadium-based oxides increase their potential utility for applications such as lighting, gas sensing, electrochemical, and photocatalysis [1–3], as well as for phosphorus applications, because they exhibit at long-wavelength excitation and chemical stability [4,5]. Thus, many vanadates have been studied for their broadband emission properties, making them a promising material for white-light-emitting diodes (WLEDs) [6–8]; furthermore, they display superior properties, such as high bright-light emission and long service lifetimes. In particular, vanadate groups ($[VO_4]^{3-}$) present in the lattices of vanadium-based oxides display a wide emission range in the visible spectral region, because of owing to their self-activated emitting properties [9] that correspond to two typical charge transitions. The luminescence is usually generated by the charge transfer transition from the 2*p* orbital of oxygen to the 3*d* orbital of vanadium. Additionally, the emission wavelength depends on the presence of metallic cations between $[VO_4]^{3-}$ groups [7,10]. The high photoluminescence (PL) emission efficiency has been examined and justified in terms of structural distortions in the V–O bond and the O–V–O bending motions of the $[VO_4]$ tetrahedron, as building blocks forming the structure of the material; these distortions yield a symmetry-breaking process within the $[VO_4]$ tetrahedron clusters. Consequently, the distortions increase the likelihood of spin-forbidden transitions compared that in isolated and ordered $[VO_4]$ clusters [4,7]. These structural distortions of the $[VO_4]$ tetrahedra may cause energy level shifts in both ground and excited states, leading to the material emitting different luminescent colors [7]. Huang et al. observed that larger distortions of the $[VO_4]^{-3}$ groups

* Corresponding author.
E-mail address: elson.liec@gmail.com (E. Longo).
[1] Permanent address: Departamento de Química Física, Universitat de València, 46100, Burjassot, Spain.

https://doi.org/10.1016/j.jlumin.2019.116990
Received 6 July 2019; Received in revised form 19 December 2019; Accepted 21 December 2019
Available online 27 December 2019

increases the probability of charge transfer processes occurring [4]. This structural change causes the parity-forbidden d-d transition of vanadium to become partially parity-allowed; additionally, the spin-forbidden $^3T_2$ ($^3T_1$) – $^1A_1$ state transition become partially allowed due to the mixing of $^3T_2$ ($^3T_1$) states with high-energy excited singlet states.

Different synthetic methods were used to obtain the $Ca_{10}V_6O_{25}$ superstructure examined herein. Previous research detailed a hydrothermal method for synthesizing calcium vanadate under temperature conditions of 120–180 °C for 24 h at pH = 12.5 [11–13]. By using this method, researchers noted modifications in the crystalline structure due to the increase of the temperature and hydrothermal reaction time. These modifications led to more intense diffraction peaks and consequently to greater crystallinity. Li et al. used a precipitation method to obtain $Ca_{10}V_6O_{25}$; they determined a series of ideal conditions for the reaction, including a reaction temperature of 90 °C for a 2 h period, which resulted in an interesting column-like crystal morphology [14]. Although there are several procedures for obtaining $Ca_{10}V_6O_{25}$, the microwave-assisted hydrothermal (MAH) method is considered to be promising owing to the more manageable synthetic conditions and excellent particle size control [15]. Absorption of microwave energy causes heating of particles, which accelerates both diffusion and collision [15]. For example, in Ref. [16] $Ca_{10}V_6O_{25}$ was synthesized at a temperature of 120 °C at different times (4, 8, 16, and 32 min), observing different morphologies for the resulting material. Thus, this methodology is desirable for the preparation of $Ca_{10}V_6O_{25}$ under low-temperature conditions that provides morphology control.

Recently, we obtained $Ca_{10}V_6O_{25}$ structures through a combination of the co-precipitation (CP) and microwave-assisted hydrothermal (MAH) methods [16]. As a continuation of previous works, we investigated the luminescence properties of vanadium materials by manipulating the synthesis temperature, thus influencing the morphological, structural order/disorder at long-, medium-, and short-range on the optical properties of $Ca_{10}V_6O_{25}$. Specifically, we investigated the PL and thermal quenching properties. The materials were characterized through X-ray diffraction (XRD), Raman spectroscopy, diffuse reflectance spectroscopy in the ultraviolet/visible region (UV–vis), field emission scanning electron microscopy (FE-SEM), energy dispersive X-ray spectroscopy (EDX), and X-ray absorption near edge structure (XANES).

In this paper, we have discussed the long-range structural order/disorder effects associated with XRD and Rietveld refinement with first principle calculations. These effects are related to the spatial periodicity of the atomic arrangement for large distances in the crystal lattice. The degree of local order/disorder in the medium-range are studied by UV–vis diffuse reflectance and PL spectroscopy; these effects extend between the calcium and vanadium clusters present in the material structure. Finally, we study the structural short-range order/disorder effects by Raman and XANES spectroscopies; these short-range effects extend only to the nearest neighbors, being characterized as punctual defects in the crystal lattice.

2. Experimental methods

The $Ca_{10}V_6O_{25}$ compounds were synthesized via the CP and MAH methods according to a procedure we previously reported [16]. First, 2 mmol of NH_4VO_3 (≥99.9%, Sigma-Aldrich) was dissolved in 30 mL of distilled water and heated to 50 °C under constant magnetic stirring until complete dissolution. Separately, 1.6 mmol of $CaCl_2.2H_2O$ (99.0%, Synth) was dissolved in 30 mL of distilled water. For the CP method, the calcium and vanadium solutions were mixed, and the pH was adjusted to 12.5 via the addition of the aqueous 6 mol/L KOH solution, and the final volume was adjusted to 70 mL then heated to 100 °C. The solution remained in equilibrium at 96 °C for 1 h (sample named CP96). For the MAH method, after adjusting the pH and obtaining a final volume of 70 mL, the precipitate formed was processed for 1 h at various temperatures of 100, 120, and 160 °C, the samples were denoted as MAH100, MAH120, and MAH160, respectively. All powders were collected at room temperature, centrifuged, and washed with distilled water resulting in a pH of around 7, then subsequently dried at 60 °C for 12 h.

2.1. Characterizations

$Ca_{10}V_6O_{25}$ samples were characterized by XRD using a Rigaku-DMax/2500 PC (Japan) diffractometer, with Cu Kα radiation (λ = 1.5406 Å) in the 2θ range of 5°–75° with a scanning rate of 0.02°/min with 40 kV and 150 mA. The Rietveld refinements were performed in the General Structure Analysis System (GSAS) program, the scan speed of 6°/min for a 2θ range of 10° to 110° with 40 kV and 60 mA. The Raman spectra measurements were carried out using a Horiba Jobin-Yvon T64000 spectrometer (Japan) coupled to a CCD Synapse detector and an argon-ion laser emitting at 514 nm with a laser power of 7 mW. The spectra were measured in the 40 - 1200 cm^{-1} range. The XANES spectra were collected at the V K-edge using the D08B-XAFS2 beamline at the Brazilian Synchrotron Light Laboratory (LNLS). XANES spectra were collected in transmission mode at room temperature using a flat Si (111) double crystal monochromator, measured from 45 eV below and 75 eV above the edge, with an energy step of 0.3 eV near the edge region. To provide a good reproducibility during the collection of XANES data, the energy calibration of the monochromator was checked while the data were being collected, using a V metal foil. In addition, the data were normalized to the edge and aligned in energy, using the MAX software [17]. The FE-SEM measurements were taken using a Supra 35-VP Carl Zeiss (Germany) operated at 15 kV. The EDX mapping was recorded in the field emission scanning electron microscopy (FE-SEM) of the FEI Company, model Inspect F50. UV–vis spectra were obtained using a Varian spectrophotometer model Cary 5G (USA) in diffuse reflection mode. PL measurements at room temperature were carried out using a Monospec 27 monochromator Thermal Jarrel Ash (USA) coupled with a R955 photomultiplier Hamamatsu Photonics (Japan). A krypton ion laser Coherent Innova 200 K (line 350 nm) with laser power about 14 mW on the samples. PL measurements as a function of the temperature (30 K–300 K) were performed using a 500 M Spex spectrometer coupled with a GaAs PMT. A Kimmon He–Cd laser (line 325 nm) with laser power up to 40 mW was used as the excitation source for PL measurements.

2.2. Computational method

First principle calculations including the temperature are performed using a standard statistical-thermodynamics approach, within the limit of the quasi-harmonic approximation implemented in the CRYSTAL17 package [18], where zero point and thermal pressures are evaluated and added to the static pressure at each cell volume, to obtain the total pressure as a function of both temperature and volume. The calculated equilibrium lattice parameters optimized at the B3LYP level [19,20] were previously published [16].

3. Results and discussion

3.1. Long-range structural order: XRD and rietveld refinement

The XRD patterns showed the degree of long-range structural order/disorder for the $Ca_{10}V_6O_{25}$ obtained by the CP method at 96 °C and by the MAH method at 100, 120, and 160 °C, see Fig. 1. The $Ca_{10}V_6O_{25}$ phase corresponds to a hexagonal structure conforming to the $P6_3/m$ space group, indexed according to the JCPDS file No. 52–649 (Fig. 1a). To observe the degree of order/disorder at the long-range scale, a full width at half maximum (FWHM) measurement was performed for the (211) and (300) planes (Fig. 1b), since the diffraction peaks result from the lattice parameters—namely, atom arrangement and periodicity over long distances. For a perfectly ordered crystal structure at long-range, the observed peaks are sharp and intense [21,22]. The sample

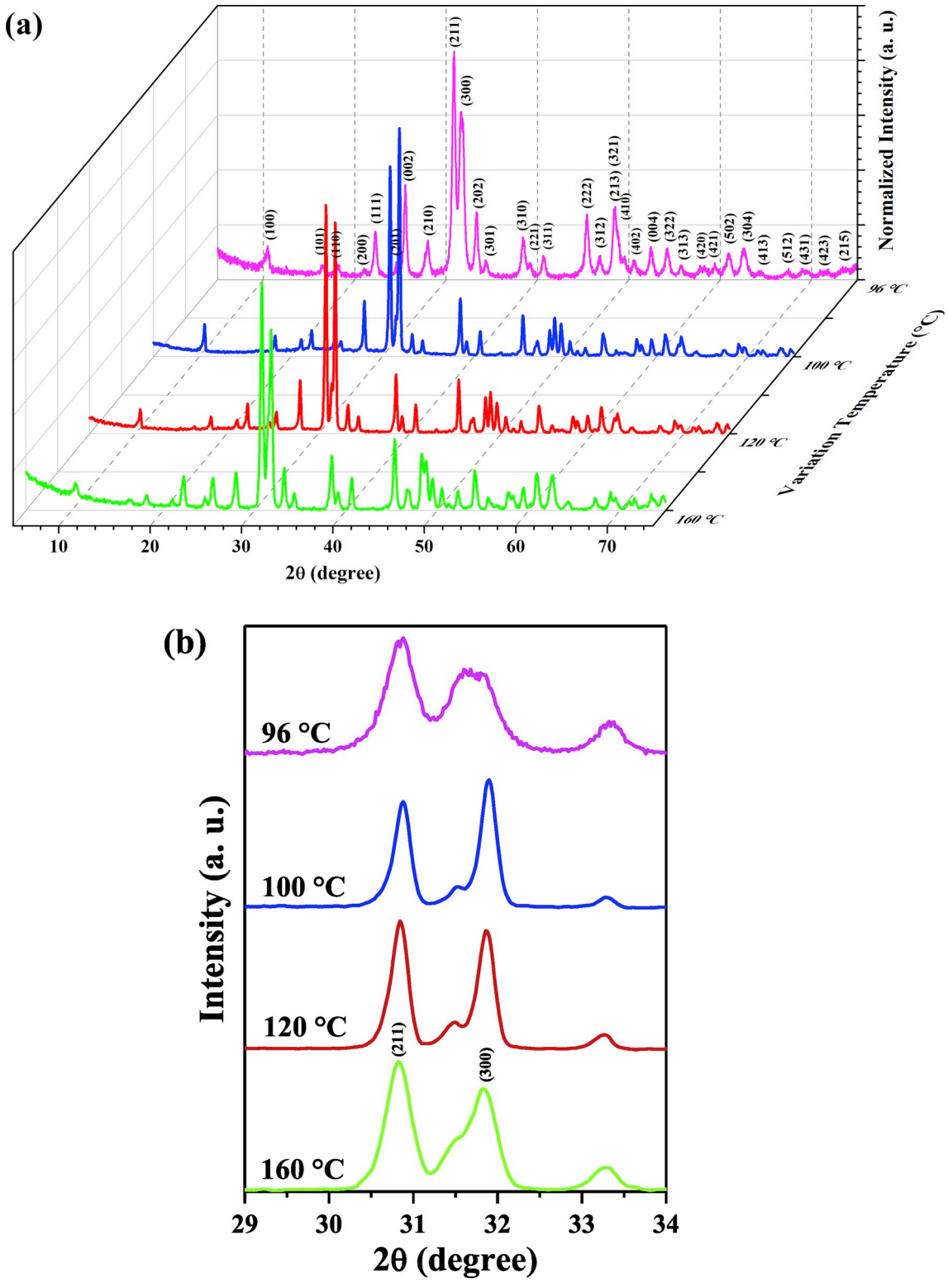

Fig. 1. (a) XRD patterns of the $Ca_{10}V_6O_{25}$ samples and (b) Magnification of the (211) and (300) planes for samples obtained by the CP method at 96 °C and the MAH method at temperatures of 100, 120, and 160 °C.

obtained using the CP method (CP96) exhibited less-defined peaks in the 29–34° range, with a FWHM value of 0.41° (211) and 0.69° (300). Thus, this material presented with structural distortions along the Ca–O and V–O bonds lengths, as well as the O–Ca–O and O–V–O bond angles, generating distorted $[CaO_6]_d$ and $[VO_4]_d$ clusters. For the MAH100 and MAH120 samples, FWHM values of 0.24° (211), 0.22° (300) and 0.24° (211), 0.24° (300) were observed, respectively; the MAH160 sample obtained at 160 °C exhibited an increase in the FWHM values at 0.36° (211) and 0.52° (300). The materials that were subjected to microwave radiation favored the crystallization and displayed long-range structural ordering. Thus, the samples obtained by the MAH method exhibited more defined peaks than those obtained by the CP method. In this way,

the higher FWHM value observed for the CP96 sample is indicative of higher structural disorder at long-range; thus, it was likely to result in higher energy (eV) of the PL emission properties. However, in the MAH system, a temperature increase to 160 °C resulted in dissolution and recrystallization of the sample, creating long-range disorder in the structure that resulted in an increased FWHM value for the MAH160 sample. Such long-range disorder causes disturbances in the crystal lattice that alter the value of the band gap energy and, consequently, alter the PL spectra.

It was observed that temperature variations provoked changes of the planes, manifested in the XRD patterns, that can be associated with differences in the crystallographic orientation. Fig. 1a shows an inversion in intensity in some planes for the CP96 sample, as observed for the 25.5° peak corresponding to the (002) plane. Thus, temperature has a strong influence on surface modification that will be preferentially exposed in the material.

The Rietveld refinement calculation method was performed using the GSAS program [23,24]. Fig. S1 and Table S1 (see Supplementary Information) show the modifications to the experimental lattice parameters and unit cell volumes of the $Ca_{10}V_6O_{25}$ samples, with respect to influences of the respective synthetic method and reaction temperatures. The $Ca_{10}V_6O_{25}$ structure does not have a Crystallographic Information File (CIF), so a card presenting the same structure (hexagonal) and space group ($P6_3/m$) was used. The Inorganic Crystal Structure Database (ICSD) card No. 24100 [25] of the mineral chromate–apatite with chemical formula structural $Ca_5(CrO_4)_3OH$ was used, as it has a similar crystallographic structure. The difference between the observed (Y_{Obs}) and calculated (Y_{Calc}) XRD patterns revealed a small difference near zero, as observed in the line $Y_{Obs} - Y_{Calc}$ (see Fig. S1). The fitting parameters, R_{Bragg} e χ^2, indicate that the refinement results were reliable to describe $Ca_{10}V_6O_{25}$ structures. The structural refinement confirmed that the $Ca_{10}V_6O_{25}$ material has a hexagonal structure. Table S1 shows the lattice parameters and unit cell volumes for the $Ca_{10}V_6O_{25}$ samples, which agree with previously reported values [16].The values for the unit cell volume and lattice parameters of the sample prepared by the MAH method at 160 °C were increased compared to those of samples obtained at lower temperatures (96, 100, and 120 °C). Thus, as temperatures increased to 160 °C, changes in the structural organization of the $[CaO_6]$ and $[VO_4]$ clusters rendered reduced network symmetry and long-range ordering. Additionally, the resulting structural distortions led to defects, such as oxygen vacancies, stresses, and strains on the crystalline lattice, that affected the PL property.

Theoretical calculations were performed to identify the influence of synthesis temperature on the resultant material structure. Table 1 shows the theoretical values for the lattice parameters and the cell volume for the $Ca_{10}V_6O_{25}$ hexagonal structure at different temperatures: 80, 100, 120, 140, 160, and 180 °C [16]. The gradual increase in the synthesis temperature was shown to provoke an expansion in unit cell volume. This increased volume is in agreement with the experimental values presented in Table S1. The phonons are responsible for the appearance of structural distortions in $[CaO_6]$ and $[VO_4]$ clusters of the lattice, accounting for the unit cell expansion.

Fig. S2 displays a schematic representation of the $[VO_4]$ clusters of the $Ca_{10}V_6O_{25}$ material, the values of the corresponding bond angles are highlighted. The atomic positions and lattice parameters of the Rietveld refinement were used in the Visualization for Electronic and Structural Analysis program [26,27] to obtain the symmetry and geometry of the $[CaO_6]$ and $[VO_4]$ clusters. Different distortions can be seen for the O–V–O bond angles in the $[VO_4]$ cluster for the samples prepared at various temperatures. An ordered and symmetrical material presents $[VO_4]$ clusters of tetrahedral symmetry entirely comprised of 109.5° angles. Thus, all samples exhibited distorted bond angles of the $[VO_4]$ clusters, which reduced symmetry and affected the PL spectrum. Ca^{2+} cations are coordinated by six oxygen anions, forming three different types of polyhedral: $[CaO_6]$ clusters presenting a trigonal prism, pentagonal pyramid, and octahedral symmetry [16]. The bond angles and other geometric details of the octahedral clusters are reported in Fig. S3.

Table 1
Results obtained from theoretical calculations.

T (°C)	a = b (Å)	c (Å)	V (Å^3)
static calc.	9.672	6.979	565.42
80	9.705	6.974	568.86
100	9.706	6.974	568.95
120	9.707	6.973	569.06
140	9.708	6.973	569.19
160	9.710	6.973	569.33
180	9.711	6.973	569.48

3.2. Short-range structural order: Raman and XANES spectroscopies

The Raman spectra revealed short-range structural order/disorder for the $Ca_{10}V_6O_{25}$ material prepared at different temperatures by both the CP and MAH methods (Fig. 2). In the 351–1062 cm^{-1} range, vibrations associated with the $[VO_4]$ tetrahedron appeared [16]. The bands at 861 and 822 cm^{-1} were assigned to the symmetric stretching vibration of the V–O bond. The band at 796 cm^{-1} is attributable to the antisymmetric stretching vibration mode of the VO_4 [16]. Bands at 406, 389, and 351 cm^{-1} correspond to the bending vibration of the O–V–O bond [28,29]. Lower-frequency bands between 48 and 273 cm^{-1} are assigned to the Ca^{2+} cation displacements and lattice mode vibrations [29,30].

Raman spectroscopy is a useful technique to understand the degree of short-range structural order/disorder owing to its relationship to the local structural order in the bonding of Ca and V clusters. In this situation, the order/disorder do not extend far beyond the nearest neighbor distances, because of this are characterized by punctual defects. In a perfect crystal, the first-order Raman phonon spectrum exhibits narrow lines that correspond to the Raman allowed zone center (r-point) modes, which obey definite polarization selection rules [21]. Considering this, FWHM measurements of the intense band at 861 cm^{-1} were conducted to observe the structural modifications at a short-range for the V–O bond within the $[VO_4]$ cluster (Fig. 2b). For the MAH100, MAH120, and MAH160 samples, the FWHM values were 18.07, 17.59, and 15.14, respectively; whereas for the CP96 sample, the FWHM value was 20.03. Thus, the sample obtained by the CP method displayed a higher FWHM value, indicative of greater distortion in the $[VO_4]$ clusters of the crystal lattice. The high FWHM value is related to a large distortion of the V–O bond, decreasing the symmetry within the $[VO_4]$ cluster. Therefore, samples obtained using the MAH method featured lower FWHM values, indicating that short-range organization increased in the microwaved system as the reaction temperature increased. Short-range motions include the vibrational and rotational movements of the material, which also induces order/disorder in the V–O bond, changing the band gap values of the material; this factor as the long-range is usually responsible for the broadband nature of the PL emissions.

In the past decade, XANES spectroscopy has been used to probe the local order of several compounds and investigate their structural and electronic properties [31–39]. Fig. 3 shows the normalized V–K XANES spectra of three representative vanadium-based reference compounds (V_2O_4, V_2O_5, and Na_3VO_4) and the as-prepared $Ca_{10}V_6O_{25}$ samples examined herein. Chaurand et al. revealed that the pre-edge peak could be considered the most useful feature of the XANES spectra, permitting one to determine both the oxidation state and the symmetry of a vanadium species [40]. Indeed, several studies have reported different methods of analysis for discerning the oxidation state and symmetry of vanadium compounds [38,40–43]. In several reports, the pre-edge peak is attributed to correspond to the transition from the V 1*s* to the V 3*d* states forbidden by dipole selection rules of centrosymmetric systems, yet allowed in non-centrosymmetric systems via hybridization between V 3*d* and O 2*p* states [38,41–43].

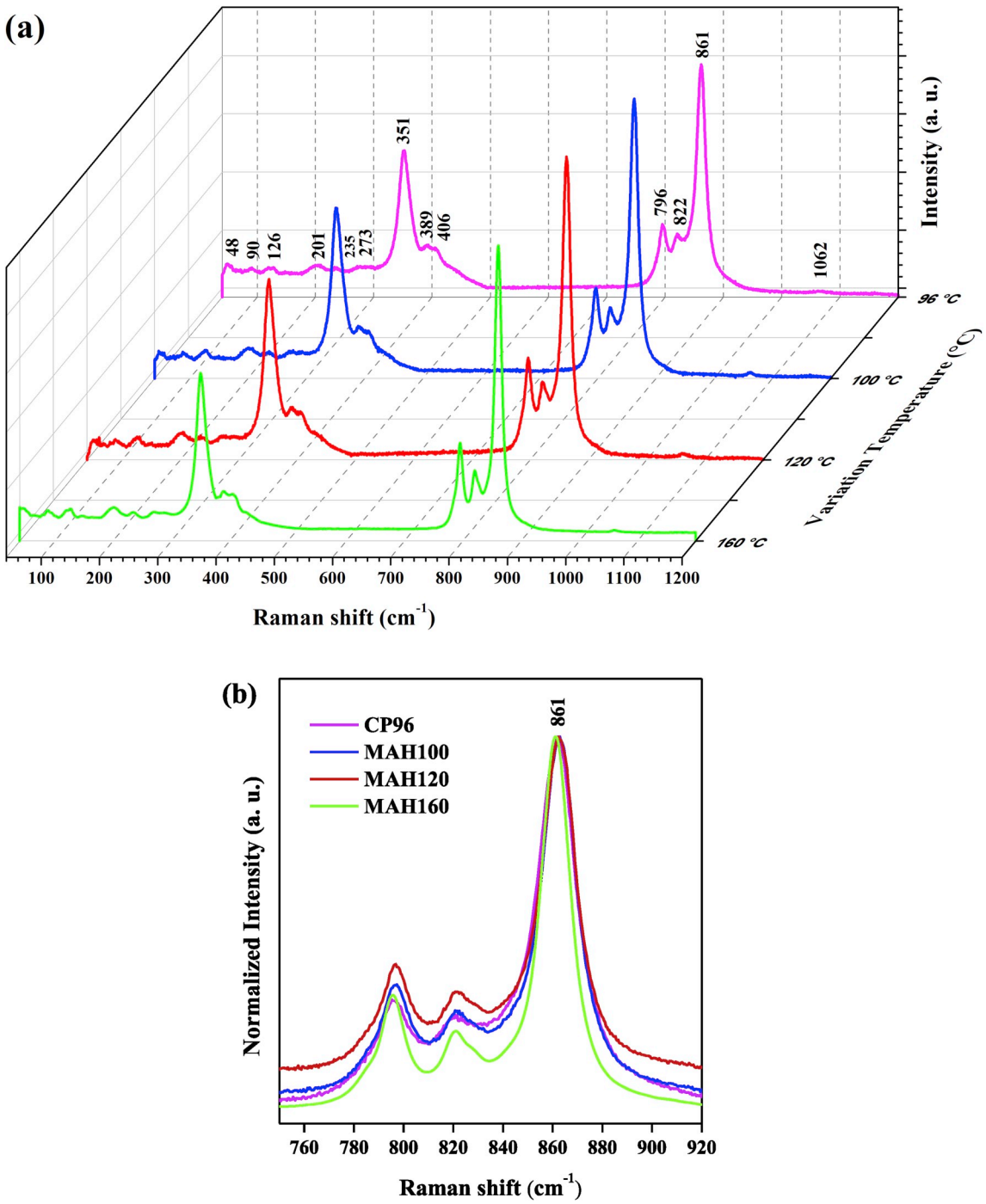

Fig. 2. (a) Raman spectra of $Ca_{10}V_6O_{25}$ samples obtained via different methods and temperature conditions. (b) Magnification of the region between 750–920 cm^{-1}.

Fig. 3a shows the difference between XANES spectra for the synthesized samples and reference compounds. Thus, the comparison of pre-edge XANES spectrum for the MAH160 sample with the reference compounds revealed similarities to the Na_3VO_4 spectrum. This demonstrates that V^{5+} atoms are present within the $[VO_4]$ tetrahedral configuration of the MAH160 sample. To verify the influence of temperature on the local structure around V^{5+} cations, the XANES spectra of $Ca_{10}V_6O_{25}$ samples are shown in Fig. 3b. The spectra of the as-prepared samples did not exhibit any significant difference, suggesting a similar local order of the V^{5+} cations for samples obtained at different temperatures.

3.3. Morphology of $Ca_{10}V_6O_{25}$

Fig. 4 illustrates the morphology of $Ca_{10}V_6O_{25}$ samples obtained via various methods and synthesis temperatures. The morphological changes of the $Ca_{10}V_6O_{25}$ crystals were a result of various synthetic temperatures. Samples prepared by the CP method at 96 °C for 1 h exhibit micrographs similar to a straw bundle that is connected to the center of the particle. The particles are microstems with a mean width of 0.08 ± 0.019 μm. When the material was subjected to MAH processing at 100 °C for 1 h, the microwave radiation favored a definition of the stems with a mean width of 0.083 ± 0.023 μm. With an increase in temperature to 120 °C, the stems disaggregated from the straw bundles and become larger, displaying a mean width of 0.802 ± 0.202 μm. At a

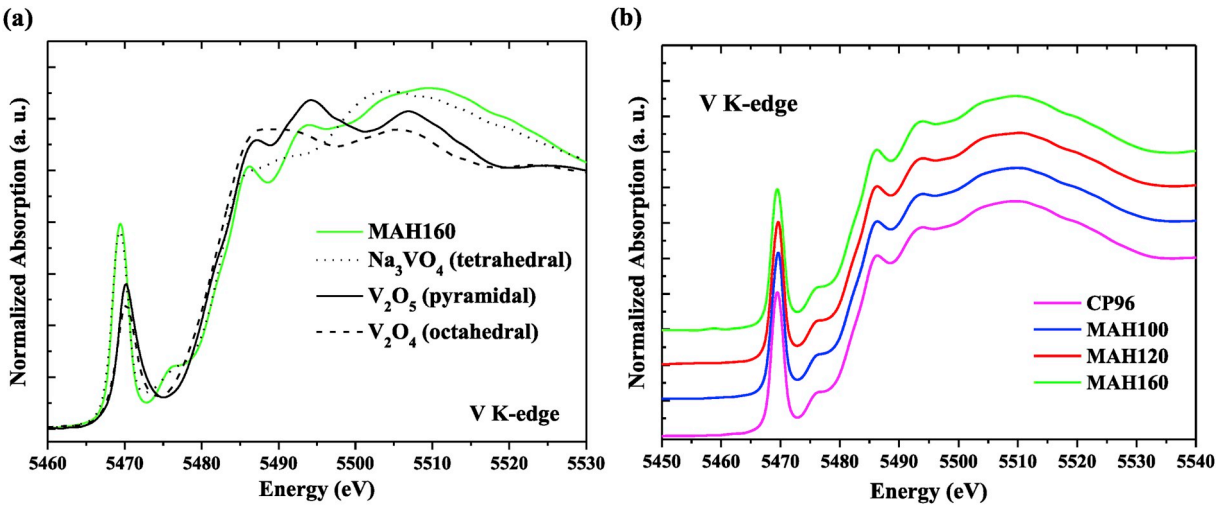

Fig. 3. Normalized V–K edge XANES spectra of $Ca_{10}V_6O_{25}$ samples. (a) XANES spectra of reference compounds and $Ca_{10}V_6O_{25}$ treated at 160 °C. (b) Samples treated at various temperatures.

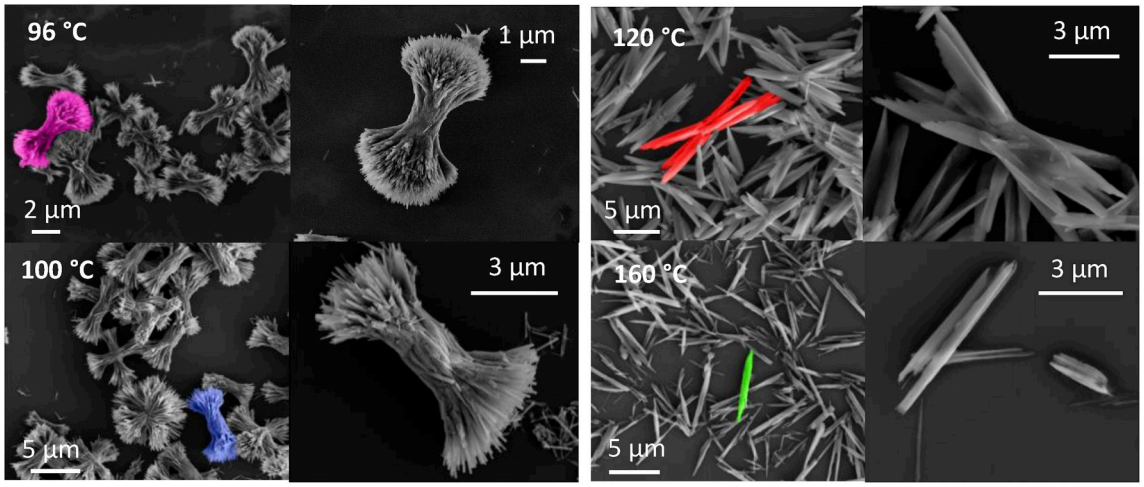

Fig. 4. FE-SEM images for $Ca_{10}V_6O_{25}$ material obtained by the CP method at 96 °C and MAH method at temperatures of 100, 120, and 160 °C.

reaction temperature of 160 °C using the MAH method, the microwave radiation favored a greater disaggregation of stems as the dissolution and recrystallization of the particle. The stems had a mean width of 0.231 ± 0.091 µm.

In the CP method, there is a high degree of disorder of the particles because the effective shocks between hydrated ionic clusters are random in nature. The crystal grows randomly and with a high defect density. When these crystals are treated in the MAH method, there is a continual dissolution and recrystallization. Microwaves associated with the phonon effect (temperature) directly influence the order and disorder of the crystal surfaces, generating a new agglomeration order in the polycrystalline system. Our observations indicate that the crystals decrease in interaction and growth. Therefore, the increase in reaction temperature and the microwave radiation for the MAH-derived samples caused a decrease in the interaction of the stems, and the straw bundle morphology was undone.

All samples exhibited the formation of stems, involving the presence of growth processes to render different 1D morphologies. Specifically, the microwave radiation used during the MAH method greatly influences the morphology of the resulting particles. Effective shocks and particle growth are altered in an open system (i.e., CP method) and a closed system (i.e., MAH method), thus altering the order/disorder at both the short- and long-range of [CaO_6] and [VO_4] clusters, effectively breaking the symmetry of clusters and changing the exposed face in morphology; as a consequence, the morphology of the $Ca_{10}V_6O_{25}$ can be modified by changing the temperature and the synthesis method.

Fig. S4 shows the chemical composition map obtained by EDX mapping for the $Ca_{10}V_6O_{25}$ samples. The images were constructed by analyzing the energy released from the emission of elemental Si, O, Ca, and V; this method indicates their distribution within the samples. In the images, green, red, yellow, and blue were used to highlight the silicon, oxygen, vanadium, and calcium, respectively. Thus, it can be observed that all the samples had a homogeneous composition of calcium, vanadium, and oxygen.

3.4. Medium-range structural order: UV–vis diffuse reflectance and PL

The optical band gap energies (E_{gap}) of the $Ca_{10}V_6O_{25}$ samples are shown in Fig. 5. The E_{gap} values of the samples were obtained by Equation (3), which relates the Kubelka–Munk (1) and Wood–Tauc (2) functions [44,45].

$$F(R) = \frac{(1-R)^2}{2R} = \frac{k}{s} \quad (1)$$

$$\alpha h\nu = C_1\left(h\nu - E_{gap}\right)^n \quad (2)$$

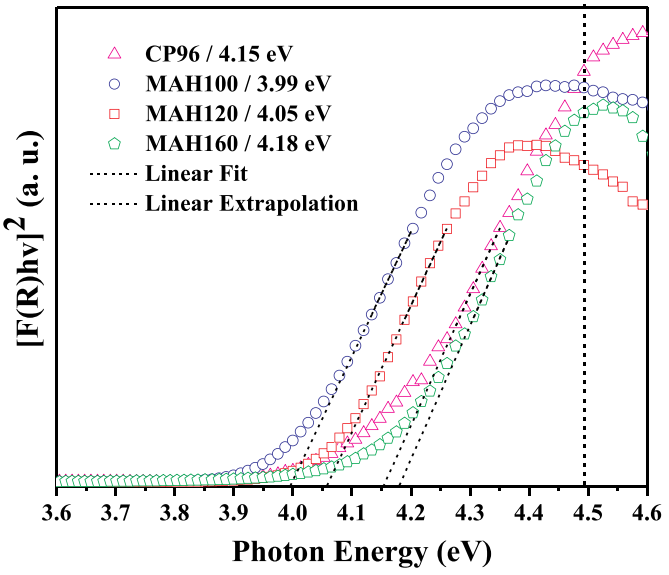

Fig. 5. UV–vis spectra for $Ca_{10}V_6O_{25}$ material obtained by the CP method at 96 °C and the MAH method at temperatures of 100, 120, and 160 °C.

$$[F(R)h\nu]^2 = C_1(h\nu - E_{gap}) \quad (3)$$

where *F(R)* is the Kubelka–Munk function of the sample, *R* is the reflectance of a thick enough layer, *k* is the molar absorption coefficient, and *s* is the scattering coefficient. In the Wood–Tauc function, α is the linear absorption coefficient of the sample, $h\nu$ is the photon energy, C_1 is a proportionality, E_{gap} is the optical band gap constant, and *n* is a constant associated with different types of electronic transitions. For the $Ca_{10}V_6O_{25}$ superstructure, a direct transition was considered; therefore, n = ½. The plot of $[F(R)h\nu]^2$ versus $h\nu$ provided the E_{gap} values by linear extrapolation of the UV–vis curve.

All $Ca_{10}V_6O_{25}$ samples exhibited near absorbance approximately 300 nm with E_{gap} values between 3.99 and 4.18 eV. All samples absorbed a high fraction of photons in the ultraviolet region. According to the Wood–Tauc theory, an ordered and crystalline material presents a sharp vertical curve (dashed curve); for the $Ca_{10}V_6O_{25}$ structure, a E_{gap} of approximately 4.5 eV would be expected. All samples had a sloped UV–vis curve, with a decrease in E_{gap} values associated with the presence of structural defects in the medium-range. An ideal semiconductor absorption should present a vertical line for an electronic transition; in contrast to that predictions, all samples had a high defect density owing to the remarkable inclination of the Urbach tail [46]. This tail appeared in disordered materials as a result of the formation of localized states (defects) extended in the band gap. It is hypothesized that these defects, resulting from short- and medium-range distortions on the $[CaO_6]$ and $[VO_4]$ clusters, perturb the energy level distribution in both the conduction band (CB) and valence band (VB); thus, the band gap values were changed. The short-range distortions propagate at medium-range by the interaction between neighboring clusters, favoring the formation of intermediary energy levels inside the band gap of materials; this commonly favors the development of broadband emission.

Fig. 6 shows the PL spectra at room temperature with a laser excitation of 350 nm, and the CIE chromaticity diagram for $Ca_{10}V_6O_{25}$ samples prepared at temperatures of 96, 100, 120, and 160 °C. The PL spectra from the $[VO_4]$ tetrahedral clusters are well established in the literature, with a broadband emission centered near 520 nm [4,6–8]. The PL property is justified by the charge transitions in the $[VO_4]$ cluster of tetrahedral symmetry, which has the ground state $^1A_1$ and excited states $^1T_1$, $^1T_2$, $^3T_1$, and $^3T_2$. The luminescence of the vanadium-based oxides is caused by charge transitions in the states ($^3T_1$, $^3T_2$) → $^1A_1$, where broadband in the visible region is defined as the 400–720 nm range. The luminescence mechanism of these materials is assigned by a charge transfer within the $[VO_4]^{3-}$ group, between the 2*p* orbital of O anion of the valence band for the 3*d* orbital of the V cation of the conduction band [4,6]. For all $Ca_{10}V_6O_{25}$ samples synthesized at different temperatures, a broadband PL with different emission centers was observed (see Fig. 6a). This is indicative that the distribution of the $[VO_4]^{3-}$ groups is not uniform in the crystal lattice, and there is a possibility of defect centers [6].

Theoretical calculations have shown that PL emissions also has an important influence on the structural distortions at the $[CaO_6]$ clusters and, especially, in the distorted tetrahedral $[VO_4]$ clusters [16]. The short-, medium-, and long-range structural order/disorder form distorted clusters $[VO_4]_d$, $[CaO_6]_d$ and ordered clusters $[VO_4]_o$, $[CaO_6]_o$; these clusters give a high probability of electron transition ($^3T_1$, $^3T_2$) → $^1A_1$. The short-range disorder forms a density of local defects in the bonds between vanadium and calcium atoms that decreases the symmetry of $[CaO_6]$ and $[VO_4]$ clusters. This intra-cluster interaction occurs by means of the polarization processes induced by the permanent dipole

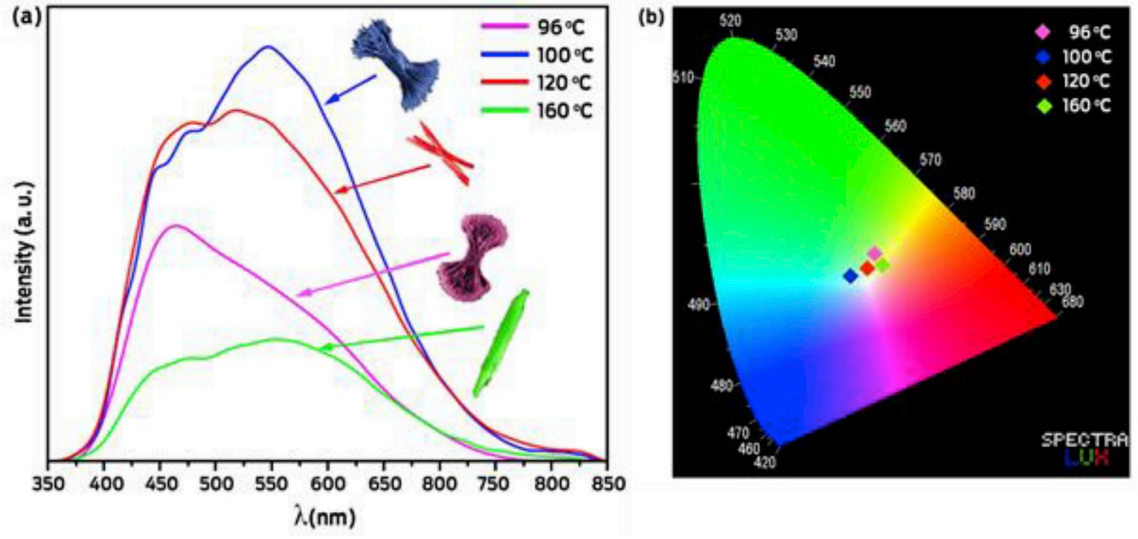

Fig. 6. (a) PL spectra at room temperature (λ_{ex} = 350 nm) and (b) CIE chromaticity coordinates of the PL spectra for $Ca_{10}V_6O_{25}$ samples obtained by the CP method at 96 °C and the MAH method at temperatures of 100, 120, and 160 °C.

moment of neighboring clusters. This interaction provokes a medium-range disorder related to the rotational motion of the permanent moments in different frameworks formed by the $[VO_4]$-$[CaO_6]$, $[VO_4]$-$[VO_4]$, or $[CaO_6]$-$[CaO_6]$ clusters. From these relationships, the structural disorder extends throughout the crystal lattice (long-range disorder) by dispersion interactions due to correlations between electrons located in the neighborhood of $[CaO_6]$ or $[VO_4]$ clusters [22,33]. Thus, the interactions between clusters with distorted symmetry, $[VO_4]_d$ and $[CaO_6]_d$, form new intermediate energy levels within the band gap of the material, favoring broadband emission. Therefore, the structural

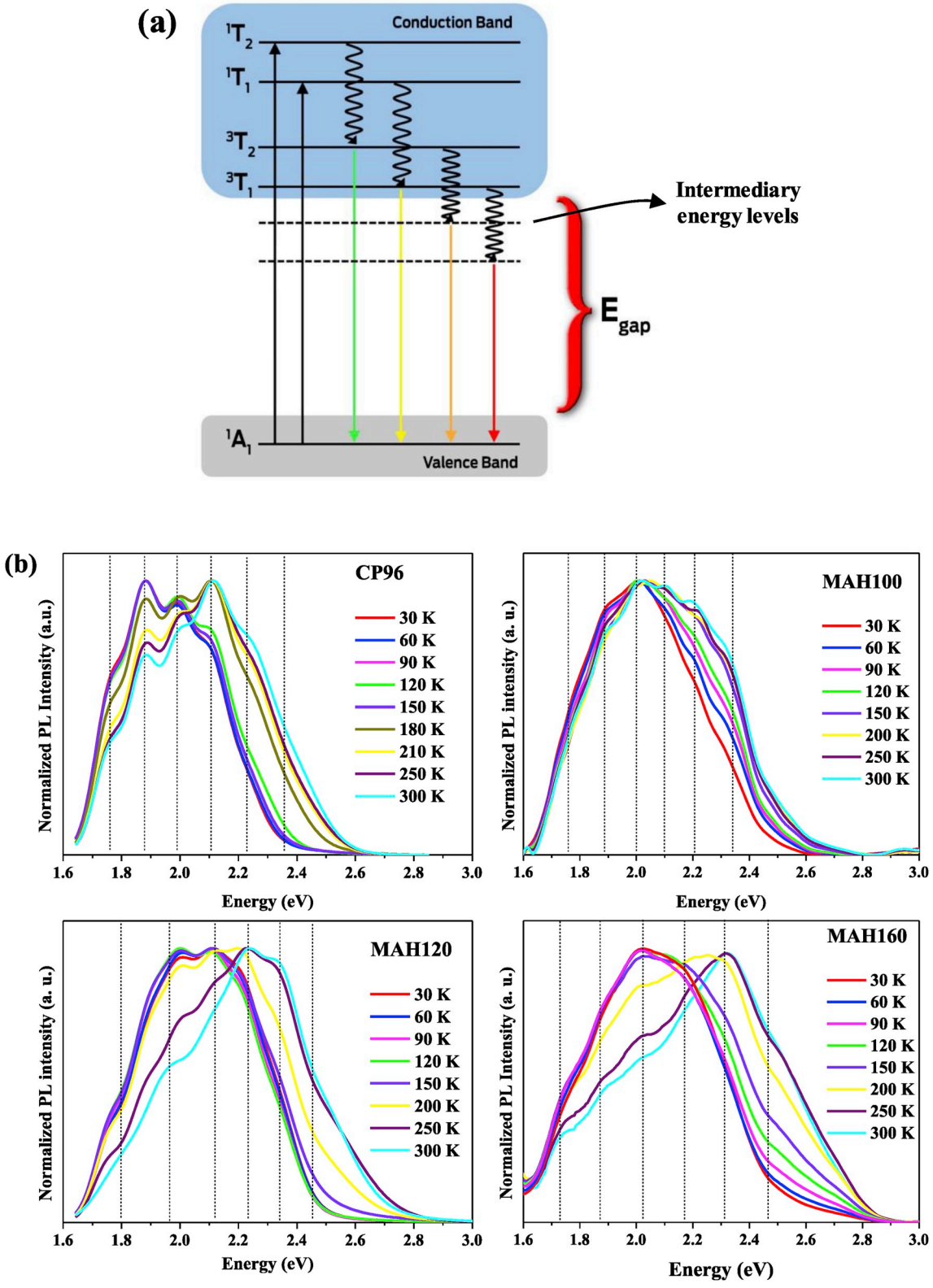

Fig. 7. (a) PL mechanism and (b) temperature dependence of the normalized PL spectra for the $Ca_{10}V_6O_{25}$ samples obtained by the CP method at 96 °C and the MAH method at 100 °C, 120 °C, and 160 °C under excitation at 325 nm.

order/disorder provokes an electronic redistribution of energy levels in both the VB and CB; these redistributions induce a change in the band gap and influence the intrinsic PL. A higher disorder structure at the long-, medium-, and short-range favored a more energetic emission for PL bands in the blue region, as was seen for the CP96 sample. The processing of samples by the MAH method at temperatures of 100 °C and 120 °C increased the crystallinity at both the long- and short-range and benefited the PL intensity for these samples. The increase in the temperature to 160 °C (MAH method) induced dissolution and recrystallization processes that separated stems from the straw bundles. Thereby, an increase in temperature during the MAH method, resulting in different PL properties. The effect of the interaction between stems was practically eliminated, although the separation of the stems caused defects on the surface of the semiconductor. The results of PL indicate a decrease in structural defects (decreased PL in the blue and green regions) with the maintenance of oxygen vacancies. Thus, disorder in both the long- and short-range induced the formation of localized defects (quantum dots disorder) in the material. A quantum dot disorder in the $[CaO_6]$ and $[VO_4]$ clusters favors the formation of different surfaces (oxygen vacancies). Therefore, particles with different morphologies and sizes exhibit different PL properties.

Variations in the reaction temperature and morphological changes in the particles have an influence on the PL properties of the resultant material. To evaluate the performance of the $Ca_{10}V_6O_{25}$ materials to emit colors via luminescence, the CIE chromaticity diagram was investigated (Fig. 6b). The PL spectrum of the CP96 sample, that with higher structural disorder at both the long and short ranges, exhibited a shift to smaller wavelengths—*i.e.*, higher energy. The CIE color coordinates conveyed that the emission was essentially green (x = 0.364 and y = 0.387). Samples prepared by the MAH method favored displacement to higher wavelengths and lower energy and favored long-, medium-, and short-range order–disorder equilibria within the crystal structure of the MAH100 and MAH120 samples. Thus, MAH samples showed emissions in the white region, as indicated by the CIE color coordinates, MAH100 (x = 0.311 and y = 0.348) and MAH120 (x = 0.350 and y = 0.368). According to the literature, CIE coordinates of the more balanced white-light region of the diagram are in the ranges x = 0.28–0.35, y = 0.30–0.37 [47,48]. Thus, the samples produced by reaction temperatures of 100 °C and 120 °C have chromatographic coordinates corresponding to a pure white-light-emitting material. Increased temperatures (160 °C) used during MAH-based synthesis, resulting in the MAH160 sample, increases the long-range disorder of the crystal lattice. Thus, a shift in the chromatographic coordinates was observed to x = 0.374 and y = 0.375; this shift is indicative of the white emission being nearer the yellow region. In this way, the different distortions in long-, medium-, and short-range for both the $[VO_4]$ and $[CaO_6]$ clusters modulate the luminescence properties of $Ca_{10}V_6O_{25}$ samples prepared by various methods and temperatures.

Fig. 7 shows the normalized PL spectra for the $Ca_{10}V_6O_{25}$ samples as a function of the temperature in the range of 30–300 K $Ca_{10}V_6O_{25}$ samples prepared by different synthesis temperatures have similar emission bands. Thus, these transitions (PL bands) are characteristic of the material structure. To understand in more detail its properties, the temperature dependence of these PL bands was investigated for all samples. A reduction of linewidth was observed at lower temperatures (<150 K), see Fig. 7b, as expected. Enhancement of PL intensity and dominance of the red emission band were also noted at lower temperatures; this red emission is usually attributed to defects of oxygen vacancies in the material or an increase in the V–O bond length to decrease the values of the transition energies ΔE [4,49,50]. Fig. S5 indicates that all $Ca_{10}V_6O_{25}$ samples display an increase in V–O bond length to values between 1.76 and 1.82 Å, favoring the formation of oxygen vacancies and, consequentially, structural distortions at the $[VO_4]$ clusters. Furthermore, distinct organizations of intermediary energy levels within the band gap contribute to the luminescence in the red and orange coordinate regions, see Fig. 7a. Higher-energy emission bands dominate at higher temperatures, see Fig. 7b. The increase in temperature has likely favored bluish-green and yellow luminescence, characteristic of an electronic transition within the $[VO_4]$ cluster, notably the transition of states ($^3T_1$, $^3T_2$) → $^1A_1$, Fig. 7a [5–7,51]. Thermally active phonons may have facilitated the excitation electrons previously trapped in oxygen's 2*p* orbital to the 3*d* orbital of vanadium. At temperatures above 150 K, the transition in PL bands of more energetic levels is favored.

All $Ca_{10}V_6O_{25}$ samples exhibited transitions corresponding to the $[VO_4]$ cluster, but with small displacements in the emission centers that are indicative of possible differences in the microstructural organization of the $[VO_4]$ tetrahedron via various distortions, as was noted by the Rietveld refinement. These distortions in the $[VO_4]$ cluster are strongly influenced by order/disorder effects in $[CaO_6]$ clusters (Fig. S3).

All samples presented a decrease in the emission intensity when the temperature was increased from 30 to 300 K (Fig. S6) [4,6,52]. The observed thermal quenching of the phosphors may be explained by the schematic diagram shown in Fig. 8a [53]. As previously shown in Fig. 7, the excited state of the $[VO_4]^{-3}$ group is exists as two near-degenerate energy levels (^1T and ^3T) [4,5,8]. The excited electron from the ground state (point 1) to the ^1T level of the excited state (point 2) and is generally transferred to the ^3T energy level (point 4); after reaching the ^3T state, the electron then returns to the ground state (point 5) by a radiative transition, as illustrated in Fig. 8a. However, when the temperature is increased, the electron may return to the ground state (^1A) by means of a non-radiative transition. Thus, the electron is thermally activated from Point 4 in the schematic to the crossover of the excited state and the ground state at Point 6. Therefore, the excited electron can easily transfer to the ground state by non-radiative means via energy transfer of phonon; thus, increasing temperatures quench emission transition from Point 4 to Point 5. As a consequence, the luminescence intensity of the phosphor decreases via a processes referred to as "thermal quenching" [53–55]. The energy required to thermally activate the excited electron from Point 4 to Point 6 via activation energy, ΔE_a, can be obtained by:

$$I(T) = \frac{I_0}{1 + \gamma e^{-\frac{E_{at}}{k_B T}}}$$

where k_B is the Boltzmann constant (8.617×10^{-5} eV K^{-1}), I_0 is the photoluminescence intensity of the $Ca_{10}V_6O_{25}$ samples at 0 K, I(T) is intensity at a given temperature, γ is the ratio between radioactive and nonradioactive lifetimes, and E_{at} is the activation energy of the thermal-quenching process. Generally, a lower value of ΔE_a leads to a higher probability of non-radiative transitions.

Fig. 8b and c shows the Arrhenius plots for all observed emission bands within the PL spectra for the MAH120 sample. The obtained activation energy is approximately 2 meV for all bands of the $Ca_{10}V_6O_{25}$ sample produced by the MAH method at 120 °C. Similar values were also obtained for all other samples (see the Supplementary Information), indicating important non-radiative transitions occurring within $Ca_{10}V_6O_{25}$.

4. Conclusion

To explore the use of promising new phosphorescent compounds, we report on the successful synthesis of $Ca_{10}V_6O_{25}$ structures with various morphologies via the CP and MAH methods at different temperatures. XRD patterns, Rietveld refinement, and Raman spectroscopy were all used to confirm the formation of a $Ca_{10}V_6O_{25}$ compound with a hexagonal structure that displays different degree of order/disorder at both short and long ranges. XANES spectroscopy revealed the presence of V^{5+} coordinated by four oxygen atoms in a tetrahedral configuration. FE-SEM images showed that variation in the temperature was favorable to obtain $Ca_{10}V_6O_{25}$ with different morphologies, an increase in temperature to 160 °C caused a decrease in interactions between particles, thereby modifying the morphology. EDX mappings showed that all

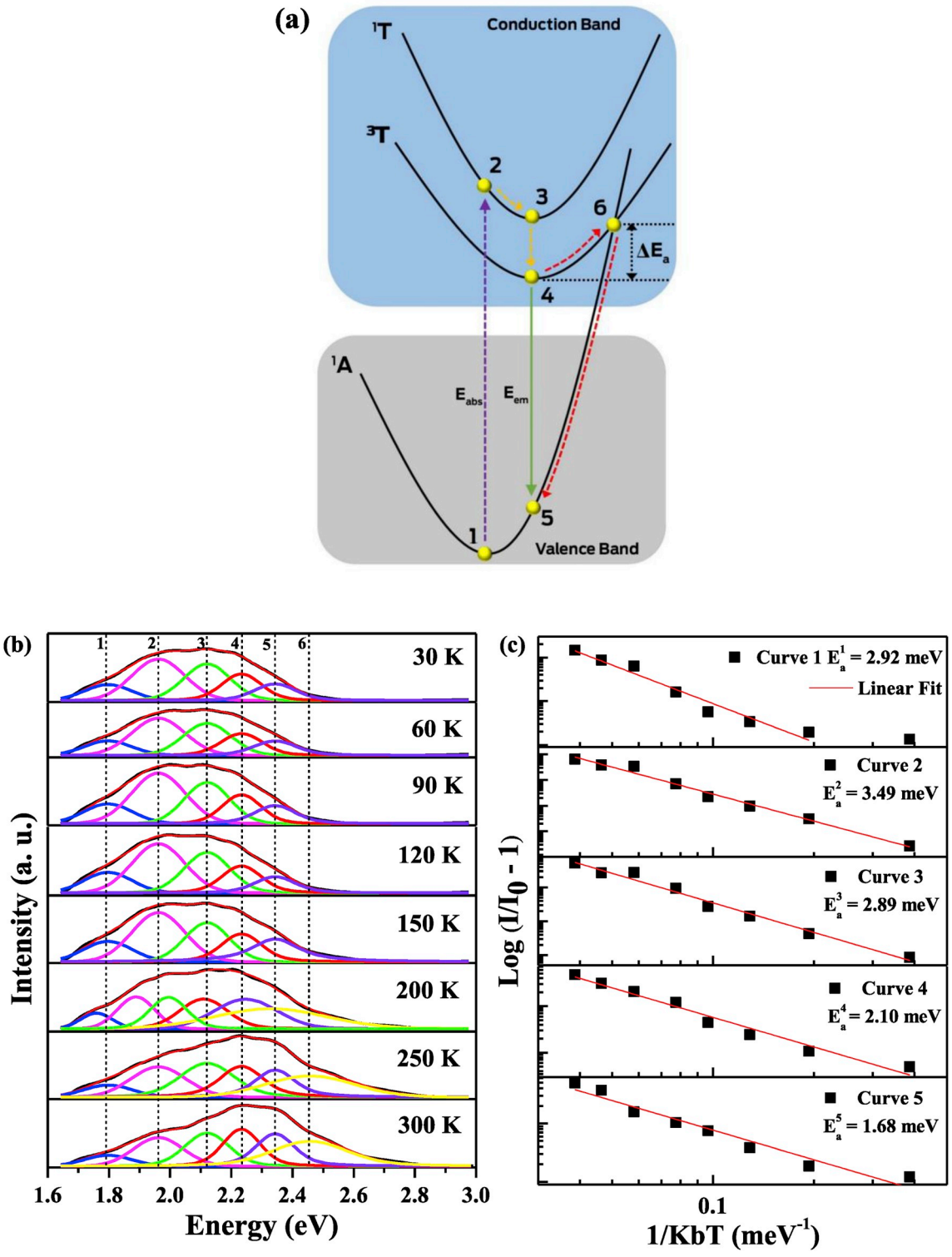

Fig. 8. (a) Electronic transition diagram of the $[VO_4]^{3-}$ group. (b) Deconvolution of the PL band spectrum using the Voigt Area G/L function. (c) Arrhenius plots of log ((I_0/I) - 1) versus 1/k_BT. The $Ca_{10}V_6O_{25}$ sample obtained by MAH method at 120 °C.

samples had a homogeneous distribution of elemental Ca, V, and O. UV–vis DRS measurements revealed that all samples displayed a medium-range lattice disorder responsible for broadband emissions. Thus, the samples presented different morphologies and structural order/disorder that favorably produced optical properties beneficial for white-light application. Therefore, distortions in the lattice and changes in the morphology of $Ca_{10}V_6O_{25}$ can tune the electronic transitions within the material through the formation of energy states within the band gap; this state benefits the broadband PL emission, which involves the participation of numerous photons generating a white-light emission that is potentially applicable in UV chip excited WLEDs. However, for this application more research to realize practical UV chip excited WLEDs is necessary.

Declaration of competing interest

The authors declare no competing financial interest.

CRediT authorship contribution statement

Mayara Mondego Teixeira: Conceptualization, Methodology, Validation, Investigation, Writing - original draft, Supervision, Writing - review & editing. **Yara Galvão Gobato:** Conceptualization, Writing - original draft, Resources, Supervision, Writing - review & editing. **Lourdes Gracia:** Formal analysis, Writing - original draft, Resources, Writing - review & editing. **Luís Fernando da Silva:** Writing - original draft, Resources, Writing - review & editing. **Waldir Avansi:** Writing - original draft, Resources, Writing - review & editing. **Marcelo Assis:** Methodology, Writing - original draft, Writing - review & editing. **Regiane Cristina de Oliveira:** Conceptualization, Methodology, Writing - review & editing. **Gabriela Augusta Prando:** Formal analysis, Investigation, Writing - review & editing. **Juan Andrés:** Conceptualization, Writing - review & editing, Supervision. **Elson Longo:** Conceptualization, Data curation, Writing - review & editing, Supervision, Project administration.

Acknowledgements

This study was financed in part by the Coordenação de Aperfeiçoamento de Pessoal de Nível Superior - Brasil (CAPES) - Finance Code 001 and financial support of agencies: FAPESP-CDMF (2013/07296–2), FAPESP (2018/01808–5), CNPq (166281/2017–4), Generalitat Valenciana for PrometeoII/2014/022, ACOMP/2015/1202, Ministerio de Economia y Competitividad, project CTQ2015-65207-P, and Universitat Jaume I″ project No. UJI-B2016-25. This research was partially performed at LNLS (project XAFS2-20180338), Campinas, SP, Brazil. The authors thank Enio Longo for the support with the scientific illustrations. The authors also thank the Servei d'Informática, Universitat Jaume I, for generous allocation of computer time.

Appendix A. Supplementary data

Supplementary data to this article can be found online at https://doi.org/10.1016/j.jlumin.2019.116990.

References

[1] C.V. Subba Reddy, I.-H. Yeo, S.-i. Mho, Synthesis of sodium vanadate nanosized materials for electrochemical applications, J. Phys. Chem. Solids 69 (2008) 1261–1264.
[2] Z. Zhang, Y.V. Kaneti, X. Jiang, A. Yu, Hydrothermal synthesis of sodium vanadium oxide nanorods for gas sensing application, Sens. Actuators B Chem. 202 (2014) 803–809.
[3] R. Yu, N. Xue, S. Huo, J. Li, J. Wang, Structure characteristics and photoactivity of simultaneous luminescence and photocatalysis in CaV_2O_6 nanorods synthesized by the sol–gel Pechini method, RSC Adv. 5 (2015) 63502–63512.
[4] Y. Huang, Y.M. Yu, T. Tsuboi, H.J. Seo, Novel yellow-emitting phosphors of $Ca_5M_4(VO_4)_6$ (M=Mg, Zn) with isolated VO_4 tetrahedra, Opt. Express 20 (2012) 4360–4368.
[5] E. Cervantes-Juárez, A.N. Meza-Rocha, R. Licona-Ibarra, U. Caldiño, E. Alvarez-Ramos, J.G. Quiñones-Galván, R. Lozada-Morales, Spectroscopy evaluation of crystalline and amorphous $Cd_2V_2O_7$ as blue phosphors, J. Lumin. 195 (2018) 234–239.
[6] Y. Pu, Y. Huang, T. Tsuboi, H. Cheng, H.J. Seo, Intrinsic $[VO_4]^{3-}$ emission of cesium vanadate $Cs_5V_3O_{10}$, RSC Adv. 5 (2015) 73467–73473.
[7] T. Nakajima, M. Isobe, T. Tsuchiya, Y. Ueda, T. Kumagai, A revisit of photoluminescence property for vanadate oxides AVO_3 (A:K, Rb and Cs) and $M_3V_2O_8$ (M:Mg and Zn), J. Lumin. 129 (2009) 1598–1601.
[8] X. Nie, W. Wulayin, T. Song, M. Wu, X. Qiao, Photoluminescence enhancement of self-activated vanadate $NaMg_4(VO_4)_3$ by cation substitutions, Mater. Lett. 185 (2016) 588–592.
[9] L. Li, W. Wang, Y. Pan, Y. Zhu, X. Liu, H.M. Noh, B.K. Moon, B.C. Choi, J.H. Jeong, Preferential occupancy of Eu^{3+} and energy transfer in Eu^{3+} doped $Sr_2V_2O_7$, $Sr_9Gd(VO_4)_7$ and $Sr_2V_2O_7/Sr_9Gd(VO_4)_7$ phosphors, RSC Adv. 8 (2018) 1191–1202.
[10] T. Nakajima, M. Isobe, T. Tsuchiya, Y. Ueda, T. Manabe, Correlation between luminescence quantum efficiency and structural properties of vanadate phosphors with chained, dimerized, and isolated VO_4 tetrahedra, J. Phys. Chem. C 114 (2010) 5160–5167.
[11] L.Z. Pei, Y.Q. Pei, Y.K. Xie, C.Z. Yuan, D.K. Li, Q.-F. Zhang, Growth of calcium vanadate nanorods, CrystEngComm 14 (2012) 4262.
[12] L. Pei, Y. Pei, Y. Xie, C. Fan, D. Li, Q. Zhang, Formation process of calcium vanadate nanorods and their electrochemical sensing properties, J. Mater. Res. 27 (2012) 2391–2400.
[13] M. Hojamberdiev, M.S. Bozgeyik, A.M. Abdullah, M.F. Bekheet, G. Zhu, Y. Yan, Y. Xu, K. Okada, Hydrothermal-induced growth of $Ca_{10}V_6O_{25}$ crystals with various morphologies in a strong basic medium at different temperatures, Mater. Res. Bull. 48 (2013) 1388–1396.
[14] L. Li, S. Zheng, S. Wang, H. Du, Y. Zhang, Thermal hydrolysis synthesis and characterization of monoclinic metahewettite $CaV_6O_{16}{\cdot}3H_2O$, J. Wuhan Univ. Technol.-Materials Sci. Ed. 29 (2014) 433–440.
[15] C. Aydın, Synthesis of SnO_2:rGO nanocomposites by the microwave-assisted hydrothermal method and change of the morphology, structural, optical and electrical properties, J. Alloy. Comp. 771 (2019) 964–972.
[16] M.M. Teixeira, R.C. de Oliveira, M.C. Oliveira, R.A. Pontes Ribeiro, S.R. de Lazaro, M.S. Li, A.J. Chiquito, L. Gracia, J. Andres, E. Longo, Computational chemistry meets experiments for explaining the geometry, electronic structure, and optical properties of $Ca_{10}V_6O_{25}$, Inorg. Chem. 57 (2018) 15489–15499.
[17] M. Alain, M. Jacques, M.-B. Diane, P. Karine, MAX: multiplatform applications for XAFS, J. Phys. Conf. Ser. 190 (2009), 012034.
[18] R. Dovesi, V.R. Saunders, C. Roetti, R. Orlando, C.M. Zicovich-Wilson, F. Pascale, B. Civalleri, K. Doll, N.M. Harrison, I.J. Bush, P. D'Arco, M. Llunel, M. Causà, Y. Noël, L. Maschio, A. Erba, M. Rérat, S. Casassa, CRYSTAL17 User's Manual, University of Torino, Torino, 2017, 2017.
[19] A.D. Becke, Density-functional thermochemistry. III. The role of exact exchange, J. Chem. Phys. 98 (1993) 5648–5652.
[20] C. Lee, W. Yang, R.G. Parr, Development of the Colle-Salvetti correlation-energy formula into a functional of the electron density, Phys. Rev. B 37 (1988) 785–789.
[21] A.P. Marques, F.C. Picon, D.M. Melo, P.S. Pizani, E.R. Leite, J.A. Varela, E. Longo, Effect of the order and disorder of $BaMoO_4$ powders in photoluminescent properties, J. Fluoresc. 18 (2008) 51–59.
[22] L.S. Cavalcante, V.M. Longo, J.C. Sczancoski, M.A.P. Almeida, A.A. Batista, J. A. Varela, M.O. Orlandi, E. Longo, M.S. Li, Electronic structure, growth mechanism and photoluminescence of $CaWO_4$ crystals, CrystEngComm 14 (2012) 853–868.
[23] H.M. Rietveld, Line profiles of neutron powder-diffraction peaks for structure refinement, Acta Crystallogr. 22 (1967) 151.
[24] A.C. Larson, R.B. Von Dreele, General Structure Analysis System (GSAS), National Laboratory, Los Alamos, 2001, pp. 124–213.
[25] K.A. Wilhelmi, O. Jonsson, X-ray studies on some alkali and alkaline-earth chromates (V), Acta Chem. Scand. 19 (1965) 177–184.
[26] K. Momma, F. Izumi, VESTA: a three-dimensional visualization system for electronic and structural analysis, J. Appl. Crystallogr. 41 (2008) 653–658.
[27] K. Momma, F. Izumi, VESTA3 for three-dimensional visualization of crystal, volumetric and morphology data, J. Appl. Crystallogr. 44 (2011) 1272–1276.
[28] S. Petit, T. Gode, C. Thomas, S. Dzwigaj, Y. Millot, D. Brouri, J.M. Krafft, G. Rousse, C. Laberty-Robert, G. Costentin, Incorporation of vanadium into the framework of hydroxyapatites: importance of the vanadium content and pH conditions during the precipitation step, Phys. Chem. Chem. Phys. : Phys. Chem. Chem. Phys. 19 (2017) 9630–9640.
[29] A.N. Unnimaya, E.K. Suresh, R. Ratheesh, Crystal structure and microwave dielectric properties of new alkaline earth vanadate $A_4V_2O_9$ (A = Ba, Sr, Ca, Mg and Zn) ceramics for LTCC applications, Mater. Res. Bull. 88 (2017) 174–181.
[30] A. Grzechnik, High-temperature transformations in calcium orthovanadate studied with Raman scattering, Chem. Mater. 10 (1998) 1034–1040.
[31] W. Avansi, C. Ribeiro, E.R. Leite, V.R. Mastelaro, An efficient synthesis route of $Na_2V_6O_{16}{\cdot}nH_2O$ nanowires in hydrothermal conditions, Mater. Chem. Phys. 127 (2011) 56–61.
[32] L.S. Cavalcante, N.C. Batista, T. Badapanda, M.G.S. Costa, M.S. Li, W. Avansi, V. R. Mastelaro, E. Longo, J.W.M. Espinosa, M.F.C. Gurgel, Local electronic structure, optical bandgap and photoluminescence (PL) properties of $Ba(Zr_{0.75}Ti_{0.25})O_3$ powders, Mater. Sci. Semicond. Process. 16 (2013) 1035–1045.
[33] L.S. Cavalcante, M.A. Almeida, W. Avansi Jr., R.L. Tranquilin, E. Longo, N. C. Batista, V.R. Mastelaro, M.S. Li, Cluster coordination and photoluminescence properties of α-Ag_2WO_4 microcrystals, Inorg. Chem. 51 (2012) 10675–10687.
[34] L.F. da Silva, W. Avansi, M.L. Moreira, A. Mesquita, L.J.Q. Maia, J. Andrés, E. Longo, V.R. Mastelaro, Relationship between crystal shape, photoluminescence, and local structure in $SrTiO_3$ synthesized by microwave-assisted hydrothermal method, J. Nanomater. (2012) 1–6, 2012.
[35] L. Gracia, V.M. Longo, L.S. Cavalcante, A. Beltrán, W. Avansi, M.S. Li, V. R. Mastelaro, J.A. Varela, E. Longo, J. Andrés, Presence of excited electronic state in $CaWO_4$ crystals provoked by a tetrahedral distortion: an experimental and theoretical investigation, J. Appl. Phys. 110 (2011), 043501.
[36] T.M. Mazzo, L. Mendonça da Rocha Oliveira, L.R. Macario, W. Avansi, R.d. Silveira André, I.L. Viana Rosa, J.A. Varela, E. Longo, Photoluminescence properties of $CaTiO_3:Eu^{3+}$ nanophosphor obtained by the polymeric precursor method, Mater. Chem. Phys. 145 (2014) 141–150.
[37] W. Avansi, R. Arenal, V.R. de Mendonça, C. Ribeiro, E. Longo, Vanadium-doped TiO_2 anatase nanostructures: the role of V in solid solution formation and its effect on the optical properties, CrystEngComm 16 (2014) 5021.
[38] W. Avansi, L.J.Q. Maia, C. Ribeiro, E.R. Leite, V.R. Mastelaro, Local structure study of vanadium pentoxide 1D-nanostructures, J. Nanoparticle Res. 13 (2011) 4937–4946.

[39] L.H. Oliveira, E.C. Paris, W. Avansi, M.A. Ramirez, V.R. Mastelaro, E. Longo, J. A. Varela, X.M. Chen, Correlation between photoluminescence and structural defects in $Ca_{1+x}Cu_{3-x}Ti_4O_{12}$ systems, J. Am. Ceram. Soc. 96 (2013) 209–217.
[40] P. Chaurand, J. Rose, V. Briois, M. Salome, O. Proux, V. Nassif, L. Olivi, J. Susini, J.-L. Hazemann, J.-Y. Bottero, New methodological approach for the vanadium K-edge X-ray absorption near-edge structure interpretation: application to the speciation of vanadium in oxide phases from steel slag, J. Phys. Chem. B 111 (2007) 5101–5110.
[41] A.N. Mansour, P.H. Smith, M. Balasubramanian, J. McBreen, in situ X-ray absorption study of cycled ambigel $V_2O_5{\cdot}nH_2O(n \approx 0.5)$ composite cathodes, J. Electrochem. Soc. 152 (2005) A1312.
[42] S. Stizza, G. Mancini, M. Benfatto, C.R. Natoli, J. Garcia, A. Bianconi, Structure of oriented V_2O_5 gel studied by polarized x-ray-absorption spectroscopy at the vanadium K edge, Phys. Rev. B 40 (1989) 12229–12236.
[43] M. Nabavi, F. Taulelle, C. Sanchez, M. Verdaguer, XANES and ^{51}V NMR study of vanadium-oxygen compounds, J. Phys. Chem. Solids 51 (1990) 1375–1382.
[44] B. Philips-Invernizzi, Bibliographical review for reflectance of diffusing media, Opt. Eng. 40 (2001) 1082.
[45] D.L. Wood, J. Tauc, Weak absorption tails in amorphous semiconductors, Phys. Rev. B 5 (1972) 3144–3151.
[46] F. Urbach, The long-wavelength edge of photographic sensitivity and of the electronic absorption of solids, Phys. Rev. 92 (1953), 1324-1324.
[47] D.P. Dutta, R. Ghildiyal, A.K. Tyagi, Luminescent properties of doped zinc aluminate and zinc gallate white light emitting nanophosphors prepared via sonochemical method, J. Phys. Chem. C 113 (2009) 16954–16961.
[48] H.S. Sindhu, B.V. Rajendra, N.D. Hebbar, S.D. Kulkarni, P.D. Babu, Defect induced white-light emission from Mn–doped ZnO films and its magnetic properties, J. Lumin. 199 (2018) 423–432.
[49] D. Dreifus, M.P.F. Godoy, A.C. Rabelo, A.D. Rodrigues, Y.G. Gobato, P.C. Camargo, E.C. Pereira, A.J.A. de Oliveira, Antiferromagnetism induced by oxygen vacancies in V_2O_5 polycrystals synthesized by the Pechini method, J. Phys. D Appl. Phys. 48 (2015), 445002.
[50] E. Pavitra, G.S. Raju, J.Y. Park, L. Wang, B.K. Moon, J.S. Yu, Novel rare-earth-free yellow $Ca_5Zn_{3.92}In_{0.08}(V_{0.99}Ta_{0.01}O_4)_6$ phosphors for dazzling white light-emitting diodes, Sci. Rep. 5 (2015) 10296.
[51] K.-C. Park, S.-i. Mho, Photoluminescence properties of $Ba_3V_2O_8$, $Ba_{3(1-x)}Eu_{2x}V_2O_8$ and $Ba_2Y_{2/3}V_2O_8{:}Eu^{3+}$, J. Lumin. 122–123 (2007) 95–98.
[52] J. Zhou, F. Huang, J. Xu, H. Chen, Y. Wang, Luminescence study of a self-activated and rare earth activated $Sr_3La(VO_4)_3$ phosphor potentially applicable in W-LEDs, J. Mater. Chem. C 3 (2015) 3023–3028.
[53] S.W. Kim, T. Hasegawa, M. Muto, A. Toda, T. Kaneko, K. Sugimoto, K. Uematsu, T. Ishigaki, K. Toda, M. Sato, J. Koide, M. Toda, Y. Kudo, Improvement of luminescence properties of rubidium vanadate, $RbVO_3$, phosphors by erbium doping in the crystal lattice, New J. Chem. 41 (2017) 4788–4792.
[54] Z. Lu, H. Wang, D. Yu, T. Huang, L. Wen, M. Huang, L. Zhou, Q. Wang, Synthesis and luminescence properties of a double perovskite $Ca_2LaNbO_6{:}Mn^{4+}$ deep-red phosphor, Opt. Laser. Technol. 108 (2018) 116–123.
[55] W. Chen, Y. Cheng, L. Shen, C. Shen, X. Liang, W. Xiang, Red-emitting $Sr_2MgGe_2O_7{:}Mn^{4+}$ phosphors: structure, luminescence properties, and application in warm white light emitting diodes, J. Alloy. Comp. 762 (2018) 688–696.